Particle transport in Poiseuille flow in narrow channels

Michelle E. Staben, Robert H. Davis *

Department of Chemical and Biological Engineering, University of Colorado, Boulder, CO 80309-0424, United States

Abstract

Particle-tracking experiments were performed to validate a model [Staben, M.E., Zinchenko, A.Z., Davis, R.H., 2003. Motion of a particle between two parallel plane walls in low-Reynolds-number Poiseuille flow. Phys. Fluids 15, 1711–1733] for neutrally buoyant spherical particles convected by a Poiseuille flow in a thin microchannel for particles as large as $d_p/H = 0.95$, where d_p is the particle diameter and H is the channel width (narrow dimension). The measured and predicted velocities agree within experimental error and show that a particle's velocity is more retarded when it is larger and/or closer to a channel wall. The particle distribution across the channel for a blunt entrance shows a focusing of small particles away from the walls and towards the center of the channel, whereas the particle distribution for an offset-angled entrance is slightly skewed towards the wall encountered first in the entrance region. As a result, the average particle velocities for the blunt entrance exceed those for the angled entrance. Moreover, due to the depletion of particles from the slow-moving region within one radius of the wall, the average particle velocity exceeds the average fluid velocity unless the particle diameter exceeds about 80% of the channel width.
© 2005 Elsevier Ltd. All rights reserved.

Keywords: Narrow channels; Particles; Poiseuille flow

1. Introduction

Particle transport in low-Reynolds-number flows occurs in many chemical engineering and biological processes, such as suspension processing, flow cytometry, sedimentation, membrane

---

* Corresponding author. Tel.: +1 3034927314; fax: +1 3034924341.
E-mail address: robert.davis@colorado.edu (R.H. Davis).

separations, polymer processing, and blood flow (Cox and Mason, 1971). Interest in low-Reynolds-number transport has recently increased with the explosion of research in the relatively new field of microfluidics, which is generally defined as the transport of fluids in microchannels with cross-sectional dimensions on the order of tens to hundreds of microns and lengths of centimeters (Whitesides and Stroock, 2001). Microfluidic devices are being explored for numerous applications, from DNA analysis to biosensors for the detection of pathogens to combinatorial chemistry of potential pharmacological agents (Beebe et al., 2002; Ehrlich and Matsudaira, 1999; Eteshola and Leckband, 2001). Significant research is being conducted on methods of transporting fluid and particulate samples (e.g., cells) to the various unit operations found on microfluidic devices. These unit operations include pumps (Andersson et al., 2001; Good et al., 2004; Terray et al., 2002), valves (Beebe et al., 2000; Unger et al., 2000), and mixers (Liu et al., 2000; Stroock et al., 2002; Ukita and Kanehira, 2002), all designed for use in the analyses being performed on the devices. However, to fully optimize microfluidic unit operations, a fundamental understanding of the basic fluid mechanics at the microscale is needed.

As discussed by other researchers (Beebe et al., 2002; Brody et al., 1996), the small size scales of microfluidic channels and unit operations generally yield low-Reynolds-number flows, where $Re < O(1)$. For such low Reynolds numbers, the flows can be modeled as Stokes flows. In the Stokes regime, a neutrally buoyant spherical particle will not cross streamlines while moving along the length of the channel, as seen by employing the reversibility property of the linear Stokes equations. Research on the motion of particles in microfluidic devices is important for optimization of various cell-based assays and unit operations, such as flow cytometry (Eyal and Quake, 2002; Jackson et al., 2002; Koch et al., 1999). Prior research has been conducted on methods of hydrodynamic focusing of particles away from channel walls (Zabow et al., 2002) and on tracking particles in electrically driven flows (Devasenathipathy et al., 2002), but there is still a need for a systematic study of the motion of single particles in microfluidic channels with Poiseuille flows, which would be applicable to devices that use pressure-driven flows, such as on-chip micropumps (Andersson et al., 2001; Good et al., 2004; Terray et al., 2002). In particular, in narrow microfluidic channels, the smallest cross-sectional dimension of the channel may not be much larger than the cells or other particulates being transported in the channel, and so the effects of the channel walls on the particle motion is important. Additionally, fabrication of devices and, in particular, of the entrance regions of microfluidic channels has often focused on ease of fabrication, without much consideration for the entrance geometry of the microchannel, which can lead to non-optimal distribution of particles in the microchannels.

In previous work, we used boundary-integral methods to predict the translational velocity of a particle as a function of its size and location in a narrow channel with Poiseuille flow (Staben et al., 2003). The goals of the current work are to validate the model for spherical particles and to examine the effects of entrance geometry on the particle distribution in a narrow channel. We perform particle-tracking experiments for Poiseuille flow in a deep-and-narrow channel to determine particle translational velocities and particle distributions across the channel.

2. Experimental setup and methods

Experiments were performed with rectangular channels that are 0.52 mm wide by 5.0 mm deep by 7.6 cm long. These dimensions, which are on the upper end of those used in typical microfluidic

systems, were selected so that the channel could be made with high precision and the corresponding particles are sufficiently large for accurate tracking with an optical microscope. Different particle sizes were employed, with diameters in the range of 0.05–0.5 mm. The channel width (horizontal dimension) was chosen as the narrow dimension to facilitate the optical microscopy, as described later.

2.1. Channel fabrication and experimental setup

The experimental setup is shown in Fig. 1. Straight microchannels were fabricated from $1'' \times 3''$ (2.54 cm × 7.62 cm) rectangles cut from a 0.25″ (0.635 cm) thick poly(methyl methacrylate) (PMMA) sheet. Along the longitudinal centerline of each rectangle, a straight trench of depth 5.0 mm was cut the length of the rectangle using a 0.02″ (0.508 mm) thick key cutter (Keo Company; purchased from Travers Machine Tools, Sterling Heights, MI) on a TM1 Vertical Machining Center (VMC; Haas Automation, Inc., Oxnard, CA). Two different entrance geometries were fabricated using a 0.062″ (0.157 cm) diameter carbide 4-flute end mill on the VMC: a blunt entrance with no additional cut by the end mill, and an angled entrance with 45° cuts with respect to the channel walls and the apex of the triangle 0.25″ from the end of the rectangular piece. The apex of the triangle is offset by 53 μm from the channel centerline, away from the channel wall encountered first in the entrance region. A $1'' \times 3''$ rectangle was cut from a 1/16″ (0.159 cm) thick PMMA sheet; using a cyanoacrylate adhesive (''Hot Stuff'' Gap-Filling Cyanoacrylate Adhesive Instant Glue, Satellite City, Simi, CA), this lid was sealed to the piece with the trench to form a closed channel of 520 μm × 5.0 mm in cross section. End caps with large dead volumes (6.0 mm long × 9.8 mm wide × 6.1 mm tall) and an entrance hole of 3.8 mm diameter and 6.0 mm length were also fabricated from the 0.25″ thick PMMA sheet and sealed to the ends using a plastic welder liquid (Proweld, Ambroid, Swanzey, NH). Lengths of Tygon tubing with an OD of 5/32″ (0.40 cm) and an ID of 3/32″ (0.238 cm) were used to connect the channel entrance to a syringe needle and the channel exit to a waste vial. The microchannel was placed on the microscope stage (Nikon TE300, Melville, NY) over the stage opening, with the lid side facing the objective turret underneath the stage of the inverted microscope, and was taped into place.

Particle location was measured across the narrow (horizontal) dimension of the microchannel as the distance of the particle center from one of the vertical sidewalls. A standard 4× objective (Nikon Achromat, NA 0.10, WD 30), with a depth of field of 55 μm and a working distance of 30 mm, was calibrated in the x–y dimensions (the plane of the microscope stage) using a micrometer stage reticle (Cole-Parmer Instrument Company, Vernon Hills, IL). A 4× objective was chosen as the highest power available that would permit observation of the largest particles translating at least two diameters in the viewing region of the videocamera while still allowing for accurate tracking of the small particles. The 4× objective does afford a large working depth, which is necessary for observing particles that are far removed from the bottom of the channel. Errors in measuring x–y translation of the microscope stage are less than five microns, while those found in measuring the direction along the channel depth are on the order of tens of microns, due to the large depth of field of the objective. Channels were fabricated with the width (or horizontal dimension) as the narrow dimension, due to the large depth of field. Since the particles are neutrally buoyant, the results should be applicable to any system in which the particles are
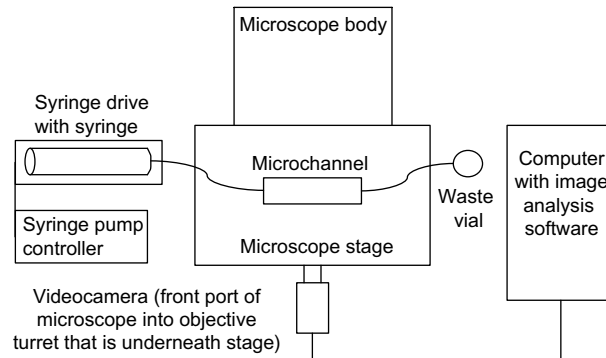
(a) Top view of experimental setup
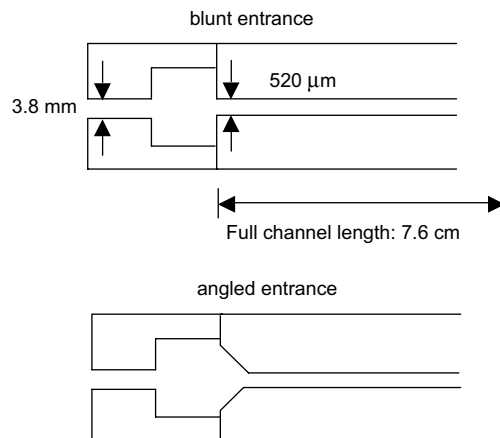
(b) Top view of microchannels (not to scale)

Fig. 1. Schematic of the experimental setup for particle velocity measurements. (a) Top view of the experimental layout. A syringe pump (left) drives flow of a particulate suspension in the microchannel on the microscope stage (center). Particle motion is imaged through the bottom of the channel using an objective mounted underneath the microscope stage (not shown) and recorded using a black-and-white videocamera connected to the front port of the inverted microscope (bottom center). Images are saved on a PC (right) and analyzed using commercial image analysis software. (b) Top view of the entrance region of the blunt-entrance (top) and angled-entrance (bottom) channels. The angles for the angled-entrance channel are 45° with respect to the channel walls. The apex of the triangular entrance is offset from the centerline by 53 μm, causing the lower wall in the diagram (right wall in experiments) of the angled-entrance channel to be encountered first in the entrance region. Dimensions shown apply for both channels.

density-matched to the surrounding fluid, even if the narrow dimension is the depth, which is more typical of microfluidic devices.

2.2. Particles and fluid

Polystyrene particles (Polysciences Inc., Warrington, PA), with diameters in the range $36 \leqslant d_p \leqslant 54$ μm ($0.07 \leqslant d_p/H \leqslant 0.10$, where d_p is the particle diameter and H is the channel

width) were employed as the small particles. The measured mean diameter, plus and minus one standard deviation, is 45 ± 4 μm for the small particles observed in the experiments. Except when the particle edge is within one diameter of the channel walls, these particles are sufficiently small to behave as tracer particles with velocities within 1% of the local undisturbed fluid velocity (Staben et al., 2003). Additional polystyrene particles (cross-linked with 5–8% divinyl benzene) were purchased (Duke Scientific, Palo Alto, CA) with a broad size range of approximately $250 \leqslant d_p \leqslant 750$ μm and sieved using U.S. Standard sieves to achieve medium particles of $240 \leqslant d_p \leqslant 280$ μm ($0.46 \leqslant d_p/H \leqslant 0.54$, with mean plus and minus one standard deviation of 260 ± 10 μm) and large particles of $410 \leqslant d_p \leqslant 495$ μm ($0.79 \leqslant d_p/H \leqslant 0.95$, with mean plus and minus one standard deviation of 440 ± 25 μm). As described later, the size range of the large particles was further subdivided by grouping direct measurements of particle diameters from the particle-tracking experiments. The density of the particles is reported by both suppliers as 1.05 g/cm^3.

A solution of 22 wt.% glycerol in water was used to achieve a fluid density of $\rho \approx 1.05$ g/cm^3. An improved density match was then obtained by titration with small amounts of water or glycerol until the particles neither sank nor floated for the ambient temperature of 23 ± 1 °C. At this temperature, the glycerol–water mixture has a viscosity of $\mu = 0.017$ g/(cm s).

2.3. Particle-tracking experiments

To initially fill the channel, a 5-mL disposable plastic syringe (Becton-Dickinson, Franklin Lakes, NJ) was filled with the desired particulate solution. A pipette tip with the narrow end cut off was slid over the syringe tip and inserted into the channel entrance tubing. The syringe plunger was then manually depressed until the channel and the exit tubing to the outlet container became filled with the solution. The plastic syringe was then replaced by a glass gastight syringe (Hamilton Company, Reno, NV) with a volume of 250 μL and an 18-gauge needle attached via a Luer-lock connection, using a 2 mm length of 3/32″ OD Tygon tubing and a plastic spacer around the needle for a snug fit in the entrance tubing. This syringe was used because it exhibits less stiction of the syringe plunger, and hence less flow-rate variability, than the Bioanalytical Systems (BAS) syringes that were purchased with the pump drive. However, increased stiction still occurred after multiple uses of a Hamilton syringe, at which time it was replaced with a new syringe. The glass syringe was attached while holding the end of the tubing below the channel to prevent introduction of air bubbles into the solution. Care was also taken to avoid the channel becoming devoid of fluid in this step. The glass syringe was then placed on the syringe drive (Baby Bee; BAS, Inc., West Lafayette, IN), connected via an RJ-45 cable to the syringe drive controller (Bee Hive; BAS, Inc.). The syringe controller dial was set to the desired flow rate in the range of $1.0 \leqslant Q_{set} \leqslant 25$ μL/min (where Q_{set} is the prescribed flow setting according to the manufacturer) and turned on. The Reynolds number, $Re = \rho Q/(D\mu)$, where $D = 0.5$ cm is the channel depth, has a maximum value of $Re = 0.05$ for the maximum flow rate of $Q = 25$ μL/min. However, most of the experiments are performed at $Q_{set} = 2.5$ μL/min, for which $Re = 0.005$.

The flow rate from the syringe pump was calibrated by tracking the smaller particles ($0.07 \leqslant d_p/H \leqslant 0.10$). To keep the particle–particle interactions small, particle concentrations of not more than 0.1% by volume were used. Images of the particles were recorded using a black-and-white videocamera (KP-M2, Hitachi Corporation, Chula Vista, CA) with a 2× intermediate magnification on the front port to which the videocamera is connected. The videocamera is connected to a

Flashbus MV frame-grabbing board (Integral Technologies, Indianapolis, IN) mounted in a Dell Dimension 8200 PC (Dell Inc., Round Rock, TX). Images of the particles are captured by the frame-grabber and saved on the PC using Metamorph imaging software (Universal Imaging Systems, Downington, PA).

The overall magnification on the computer monitor is 165×. For calibration of the syringe pump, particle velocity measurements were taken near the midpoint of the channel depth, determined by translating the objective upwards (using the coarse focus knob) from the lower surface of the channel until it is approximately 2.5 mm from the bottom of the channel (found by focusing on minute scratches on the bottom channel surface). For the Nikon TE300, one full rotation of the coarse focus knob yields 4 mm of apparent vertical objective movement with air as the imaging medium. The physical motion of the knob, and, hence, the objective, is independent of the imaging medium; however, the apparent image depth is dependent upon the refractive index of the medium. To find the corresponding image depth for a 22 wt.% glycerol-in-water solution, the refractive index of the solution, $n = d_r/d_a$, is calculated, where n is the refractive index, d_r is the real depth and d_a is the apparent depth, yielding an apparent depth of 3.7 mm for our 5.0 mm deep channel. After a startup time of a few seconds (to ensure that the syringe is operating at its prescribed setting), images of the particles at a fixed location along the channel length were grabbed at a rate of one frame per 2–3 s (longer times were used for slower flows) for an imaging period that lasts 1 min. This frame-grabbing was continued every minute for a period of 5 min, at which time the flow setting was changed. Flow settings of $Q_{set} = 1.0, 2.5$ and 5.0 μL/min were calibrated. To check the reproducibility, the flow was completely stopped and then the process was repeated. Data for the calibration experiments were taken at ∼1–4 cm from the channel entrance.

The images were analyzed using Metamorph imaging software, which has a drop-in Motion-Tracking Module. Particles in focus (which have a well-defined outline and light-colored center) are identified by the user and tracked by the software. A given particle was typically tracked for 30–60 s, or about 400–800 μm travel distance. The results, which include x–y coordinates and velocity measurements, are automatically transferred to an Excel spreadsheet. For each particle's measured translational velocity, the corresponding centerline velocity is obtained from

$$U_c = \frac{U_p}{4\frac{d}{H}\left(1 - \frac{d}{H}\right)}, \tag{1}$$

where U_c is the centerline fluid velocity calculated from a given tracer particle velocity, U_p is the measured tracer particle velocity, d is the distance of the particle center from one of the side walls, and H is the channel width. Eq. (1) is based on the parabolic formula for Poiseuille flow between two flat plates (Happel and Brenner, 1986), which is a good approximation for this large-aspect-ratio microchannel, except near the top and bottom walls. From a set of movies taken during the same time series, an average centerline velocity, $\langle U_c \rangle$, is found by averaging over all of the experimental data in the time series, and is compared to $\langle U_c \rangle$ from another time series to determine if the pump is yielding reproducible flow. Particles near the wall (outside the range of $0.14 < d/H < 0.86$) were not used in these calculations, since the particle velocity is then reduced by more than 1% from the Poiseuille fluid velocity and a small error in the measurement of the location of the particle center yields a relatively large error in the predicted centerline velocity. The predicted U_c can be calculated by using a 3D Matlab implementation of the analytical solution for fully

developed Poiseuille flow in a rectangular channel (White, 1991), using the prescribed flow rate and the channel dimensions as inputs to the program. These quantities are related by

$$Q = k\left(\frac{2}{3}U_c\right)HD, \tag{2}$$

where k is a correction factor that accounts for the presence of the top and bottom walls of the channel ($k = 1$ for Poiseuille flow between infinite parallel plates). Its value is $k = 0.94$ for the geometry employed ($H/D \approx 0.1$). This factor is used in Eq. (2) to obtain Q_{meas}, the measured volumetric flow rate based on the measured $\langle U_c \rangle$, for a given flow setting, which can be compared with the prescribed flow setting to calibrate the pump.

Particle velocity measurements for the medium and large particles were performed in a manner similar to the small-particle velocity measurements, with $Q_{set} = 2.5\ \mu L/min$ used for the medium particles and $Q_{set} = 1.0\ \mu L/min$ for the large particles. These particles were added to the fluid in low concentrations of less than 0.25% particles by volume, so that a second particle near a particle being tracked was rare (if two particles were within five diameters of each other, they were not included in the analysis). Small particles were also included as tracers, at a concentration of 0.1% by volume. The velocities of tracer particles separated by at least five diameters of the larger particles being tracked were used with Eq. (1) to find the average fluid centerline velocity, $\langle U_c \rangle$. Data for the medium and large particles were taken at $\sim$1 cm from the channel entrance.

2.4. Possible inertial lift and gravitational effects

Inertial lift could be a factor in these flows with low but nonzero Reynolds number. Inertial lift occurs due to the small but nonzero inertial terms in the Navier–Stokes equations causing particles to drift across streamlines and migrate toward an equilibrium position at $0.6(H/2)$ of the distance from the nearest wall for Poiseuille flow in tubes or between parallel plates, where H is the tube diameter or spacing between the parallel plates, respectively (Segre and Silberberg, 1961, 1962). An estimate of the inertial lift velocity normal to the primary flow direction is (Davis, 1992)

$$v_L = \frac{b\rho d_p^3 \gamma_0^2}{128\mu}, \tag{3}$$

where $\gamma_0 = 6Q/(WH^2)$ is the shear rate near the wall. The factor b has a positive sign for a small particle near one wall, implying motion away from the wall, and has a maximum value of 1.6 near the wall for slow laminar flow in a slit (Ho and Leal, 1974; Vasseur and Cox, 1976).

For the flow rates used for particle velocity measurements ($1.0 \leqslant Q_{set} \leqslant 2.5\ \mu L/min$), the inertial lift on the tracer particles causes negligible motion across the channel width ($\Delta d/H < 0.01\%$ for $Q_{set} \leqslant 2.5\ \mu L/min$, where Δd is the change in particle position across the channel width as it travels one half of the channel length). For the medium particles, $\Delta d/H$ due to inertial lift is less than 2% over the channel half-length, and less than 1% for the location 1–2 cm from the entrance at which data were taken, which is within experimental uncertainty. However, inertial lift could be a factor for the large particles, since the maximum inertial lift velocity of $v_L = 0.032\ \mu m/s$ ($b = 1.6$, $Q_{set} = 2.5\ \mu L/min$, $\rho = 1.05\ g/cm^3$, $\mu = 0.017\ g/(cm\ s)$, and $d_p = 495\ \mu m$ in Eq. (3)) would cause a particle to drift across 5% of the channel width, H, in the first 2 cm of the channel length. To reduce the effects of the inertial lift to the order of the uncertainty in measurement of the lateral

dimensions, the slowest flow rate of $Q_{set} = 1.0\ \mu L/min$ was used for velocity measurements for the large particles. In all cases, any horizontal drift during the tracking of a particle (travel distance less than 1 mm) was negligible.

For the large particles, obtaining sufficient neutral buoyancy to prevent gravitational settling is extremely difficult, due to the dependence of the terminal settling velocity on the square of the particle diameter (see Happel and Brenner, 1986, pp. 124–125):

$$v_s = \frac{d_p^2(\rho_s - \rho)g}{18\mu},\tag{4}$$

where d_p is the sphere diameter, ρ_s is the sphere density, ρ is the fluid density, g is the gravitational acceleration (980 cm/s^2), and μ is the fluid viscosity. Eq. (4) shows that a density mismatch of as little as 0.01% allows a large particle with a diameter of 495 μm on the centerline of the channel to settle (or rise) half the depth of the channel in only 0.3 cm of motion along the channel length at $Q_{set} = 1.0\ \mu L/min$. Thus, to avoid the large particles settling or rising to near the bottom or top of the channel, the flow was initially set at the highest setting ($Q_{set} = 25\ \mu L/min$) to push the large particles to the viewing area, and then reduced to $Q_{set} = 1.0\ \mu L/min$ when the particles reached the viewing region. The flow rate of $Q_{set} = 1.0\ \mu L/min$ was chosen to ensure that measurable inertial lift does not occur during the imaging process, but inertial lift may affect the position of a large particle prior to reaching the viewing area.

2.5. Particle distribution measurements

To examine the effects of entrance geometry, the distributions of the locations of the particles across the channel were obtained for both geometries. For the medium and large particles, the center locations measured by the Metamorph Motion-Tracking Module were used to obtain the particle distribution, since those center location measurements include all medium and large particles tracked in the system. For the small particles, a large amount of data on the center locations was obtained by slightly modifying the tracking method. Instead of tracking a single small particle through the entire viewing area, the interval between images was increased to 20 s to obtain a large file with many particle images. Each particle can be individually identified and thus counted only once. Moreover, the fact that the particles near the center have higher velocities (and, thus, are further apart if the particles are randomly distributed as they enter the channel) than particles near the wall does not present a bias, since all particles that pass a fixed axial location in a given time interval are counted. Distributions of the large particles are presented as a function of the gap between the wall and the closest edge of the particle to the wall, since the variation in their diameters is comparable to the variation in the possible center locations. Particle diameters were measured in Metamorph using the Calipers function.

3. Results and discussion

3.1. Pump calibration and reproducibility

Since the dimensionless measured particle velocities are dependent upon the centerline velocity used to scale them, calibration of the pump was vital to obtaining accurate results. Ideally, the

pump used would produce a constant, reproducible flow that matches the settings given by the manufacturer. For the flow rates used in the velocity measurements (to be discussed in Section 3.2), we obtained $\langle U_c \rangle = 47.9 \pm 5.5 \ \mu m/s$ (mean plus and minus one standard deviation) for 218 measurements for $Q_{set} = 5.0 \ \mu L/min$, $23.9 \pm 2.6 \ \mu m/s$ (86 measurements) for $2.5 \ \mu L/min$, and $9.8 \pm 0.8 \ \mu m/s$ (62 measurements) for $1.0 \ \mu L/min$. The corresponding flow rates from Eq. (2) with $k = 0.94$ are $Q_{meas} = 4.66 \pm 0.54, 2.34 \pm 0.26$, and $0.95 \pm 0.08 \ \mu L/min$ for $Q_{set} = 5.0, 2.5$, and $1.0 \ \mu L/min$, respectively. Thus, the measured flow rates are slightly smaller than the set flow rates, and linear regression of all of the calibration data gives $Q_{meas} = (0.94 \pm 0.01)Q_{set}$ at the 90% confidence level. The flow rate from the pump is a function of the syringe volume and the length of the syringe barrel. Since the Hamilton syringes are the same length as the BAS syringes, the stroke length of the syringe should not change the flow rate scale. The smallest syringe BAS makes is $500 \ \mu L$, even though the pump manual specifies that syringes of the range $10–5000 \ \mu L$ can be used. The BAS pump may not have been calibrated by the manufacturer for a 250-μL syringe, which could cause the observed discrepancy between the measured and predicted flow rates.

The uncertainty (due to pixel resolution) in lateral measurement of the location of the particle center is about $5 \ \mu m$ in the x and y directions (perpendicular and parallel to the flow direction, respectively), leading to a measurement uncertainty in the particle velocity of about 1–2% of its value and in the particle location across the channel of about 2% of the channel half-width. The uncertainty in particle location gives only a 1–2% error in determining the centerline velocity from measured velocities of particles near the channel center, but this error increases to 6–7% when a particle is within $75 \ \mu m$ of either wall (the closest distance used in the calibrations). Since the relative standard deviations are larger (about 10%), it appears that flow-rate fluctuations are non-negligible.

To further ascertain the constancy and reproducibility of the flow rates, Table 1 presents the results from a set of calibration experiments in which $\langle U_c \rangle$ was measured for five consecutive 1-min intervals for four different experiments with $Q_{set} = 2.5 \ \mu L/min$. Several of the observed differences in $\langle U_c \rangle$ within and between each of the 5-min experiments are significant at greater than 90% confidence. For example, the largest overall velocity of $25.0 \pm 0.7 \ \mu m/s$ is statistically different from the two smallest overall average velocities of $23.1 \pm 3.0 \ \mu m/s$ and $24.0 \pm 1.6 \ \mu m/s$, at greater than 90% confidence. Moreover, the variations appear to be random, rather than showing a systematic drift toward higher or lower centerline velocities within each 5-min interval.

Table 1
Pump calibration experiments to give the measured average centerline velocity for different intervals at $Q_{set} = 2.5 \ \mu L/min$

Interval (min)	$\langle U_c \rangle \pm$ one standard deviation ($\mu m/s$)			
0–1	24.5 ± 4.5	26.6 ± 0.8	24.3 ± 0.5	22.7 ± 1.3
1–2	26.6 ± 2.4	22.5 ± 0.6	24.9 ± 0.3	25.8 ± 0.7
2–3	23.5 ± 0.3	23.6 ± 0.5	24.7 ± 0.4	23.6 ± 0.8
3–4	23.7 ± 0.9	23.4 ± 1.0	25.5 ± 1.1	22.5 ± 3.8
4–5	25.4 ± 0.2	24.4 ± 0.6	25.4 ± 0.1	19.5 ± 4.8
0–5	24.7 ± 2.5	24.0 ± 1.6	25.0 ± 0.7	23.1 ± 3.0

Each column represents a single 5-min experiment. The first five rows are the averages for the two to five particles observed in each individual minute of the experiment, with the overall $\langle U_c \rangle$ for the entire 5-min interval in the last row.

Some variation in the values of Table 1 can be attributed to using particles away from the centerline to calculate $\langle U_c \rangle$, since (as discussed in Section 2.3) a small error in the particle's location as a function of the channel width for particles near the walls can lead to a large error in the U_c calculated from that particle's velocity. To alleviate this error, only particles in the center third of the channel are used to find $\langle U_c \rangle$ for scaling the particle velocity results (Section 3.2). For any given $\langle U_c \rangle$ used for scaling purposes, the standard deviation using only data from $0.33 \leqslant d/H \leqslant 0.67$ is on the order of 5% of $\langle U_c \rangle$ or less, which is about half that for all data from $0.14 \leqslant d/H \leqslant 0.86$ as used in Table 1.

3.2. Particle velocity measurements in blunt-entrance and angled-entrance channels

Fig. 2 shows the comparison of the measured particle velocities, scaled by the average centerline velocity (determined by the method discussed in Section 2.3), with the boundary-integral simulations of Staben et al. (2003). Good agreement is shown between theory and experiment for both entrance geometries and all three particle size ranges. The large particles are separated into three subgroups based on the scaled particle diameter, d_p/H. The two largest subgroups are shown for both entrance geometries combined, since relatively few data were collected.

Fig. 2 shows that small particles tend to move with the same velocity as the fluid, except in the regions of closest approach to the walls, where the particle velocities are slightly retarded due to
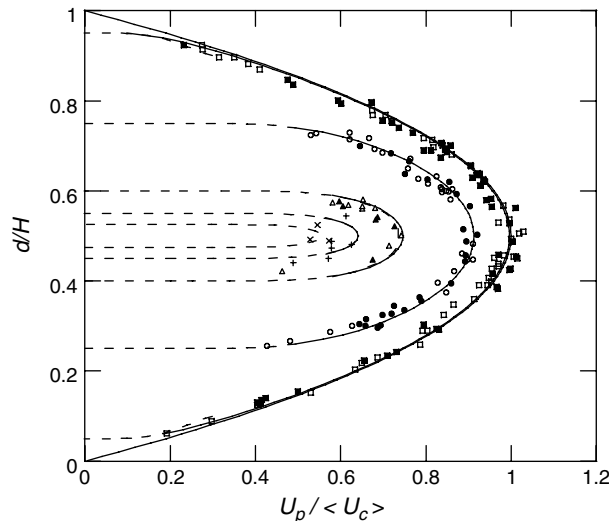

Fig. 2. Experimental measurements of the particle velocity, U_p, scaled by the average centerline velocity, $\langle U_c \rangle$, as a function of the particle center distance from one of the walls, d, scaled by the channel width, H. The solid curves are the undisturbed Poiseuille fluid velocity and simulation results (Staben et al., 2003) for particles with $d_p/H = 0.1, 0.5, 0.8, 0.9$ (right to left), and the dashed curves are the near-wall asymptotic results (Staben et al., 2003) for particles with $d_p/H = 0.1, 0.5, 0.8, 0.9, 0.95$ (bottom to top, with mirror images about $d/H = 0.5$). The symbols are for particles in the blunt-entrance channel with $0.07 \leqslant d_p/H \leqslant 0.10$ (■), $0.46 \leqslant d_p/H \leqslant 0.54$ (●), and $0.79 \leqslant d_p/H \leqslant 0.83$ (▲); in the angled-entrance channel with $0.07 \leqslant d_p/H \leqslant 0.10$ (□), $0.46 \leqslant d_p/H \leqslant 0.54$ (○), and $0.79 \leqslant d_p/H \leqslant 0.83$ (△); and in both channels for $0.88 \leqslant d_p/H \leqslant 0.91$ (+) and $0.93 \leqslant d_p/H \leqslant 0.95$ (×).

the close proximity of the wall. The particle velocity decreases with increasing particle size for a constant particle center location, due to the retarding effects of the nearby walls, as seen by the shifting of the velocity curves to the left with increasing particle size. Particle centers are physically excluded from the region within one radius of a wall due to the finite size of the particle. Moreover, the particle velocity increases rapidly over short distances of the edge of the particle from the wall (observed by the relatively flat curves in the asymptotic region in Fig. 2). As a result, the large particles have a narrow range of velocities, while the small particles experience a wide range of velocities.

While the translational velocity for a given particle size and center location is independent of the entrance conditions, the angled-entrance channel appears to allow both the small and medium particles to translate along the channel in close proximity to the channel walls more frequently than in the blunt-entrance channel (compare open and closed symbols in Fig. 2). This possible focusing of particles away from the walls in the blunt-entrance channel is examined further in the next section.

3.3. Particle distribution as a function of entrance geometry

To quantitatively examine the effects of entrance geometry, we measured the distributions of particle center locations across the channel. Fig. 3a shows the distribution of small particles in the blunt-entrance channel, with a measurable depletion of particles near the wall and excess of particles in the center of the channel. The number of particles in the first four nonexcluded bins at the left-hand side, as well as the first three nonexcluded bins at the right-hand side, are statistically lower than those for a uniform distribution of particles at the 90% confidence level, using a Poisson probability distribution to compare the uniform distribution to the measured bins. The depletion from the near-wall regions occurs because corners on the blunt entrance may prevent particles from entering the channel in close proximity to the channel walls. Similarly, the numbers of particles in the nine highest bins are statistically higher than those for a uniform distribution of particles at the 90% confidence level, which is a further indication of focusing. The excess of particles in the center of the channel is not due to overcounting of the faster-moving particles, since the experiments were performed such that each particle entering the viewing area in a given time interval could be clearly identified and counted only once towards the overall distribution, as described in Section 2.5.

Fig. 3b shows the distribution of small particles in the angled-entrance channel, with a noticeable asymmetry in the distribution. For this distribution, the first four nonexcluded bins on the left-hand side are statistically lower than a uniform distribution at the 90% confidence level, whereas only one nonexcluded bin near the right-hand side is low, indicating that particles are selectively pushed towards the wall that is encountered first in the entrance region. Particle numbers in the five highest bins are statistically higher at the 90% confidence level than for a uniform distribution.

To further examine the particle distributions, sample trajectories for small particles entering the blunt-entrance and angled-entrance channels are shown in Fig. 4a and b, respectively. The blunt-entrance results show a slight but critical focusing of particles away from both side walls and towards the center of the channel, while the angled-entrance results show more focusing of particles away from the first wall than from the second wall.
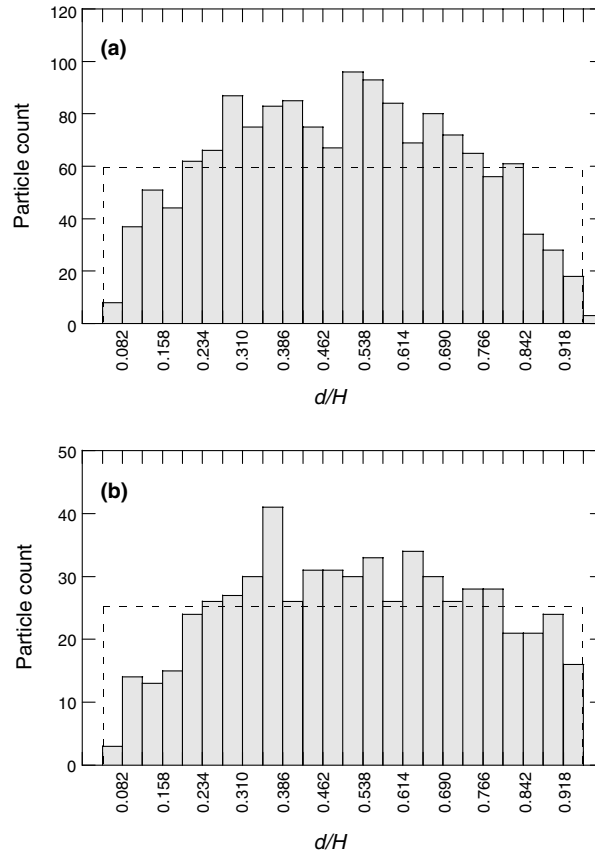
Fig. 3. (a) Frequency distribution of particles with $0.07 \leqslant d_{\mathrm{p}}/H \leqslant 0.10$ in the blunt-entrance channel. (b) Frequency distribution of the same size range of particles in the angled-entrance channel with right wall extending into entrance region. The dashed line in each plot is a uniform distribution of particles across the channel width for the number of particles in a given plot, except for the excluded region within one average particle radius of either wall. The three particles in the right-most bin of Fig. 3a are smaller than the average size.

Medium particle distributions are shown in Fig. 5. These particles are distributed nearly uniformly across the channel, and none of the bins is statistically different from the uniform distribution at the 90% confidence level. However, Fig. 2 shows that more medium particles are close to the wall for the angled entrance than for the blunt entrance. For the large particles, only those particles with $d_{\mathrm{p}}/H \approx 0.8$ were examined, since the experimental difficulties associated with attaining neutral buoyancy (Section 2.4) prevented the acquisition of enough data to examine the distribution of the largest particles across the channel width. Fig. 6 shows the distribution of large particles with $0.79 \leqslant d_{\mathrm{p}}/H \leqslant 0.83$ as a function of the separation of the particle edge from the nearest wall, calculated as the difference between the distance of the center from the nearest wall, d_{w}, and the particle radius, $d_{\mathrm{p}}/2$, scaled by the channel width, H. This distribution also shows no focusing of particles away from the wall, but instead a slight excess of particles near the wall (though only the second bin is statistically higher than the uniform distribution at the 90% con-
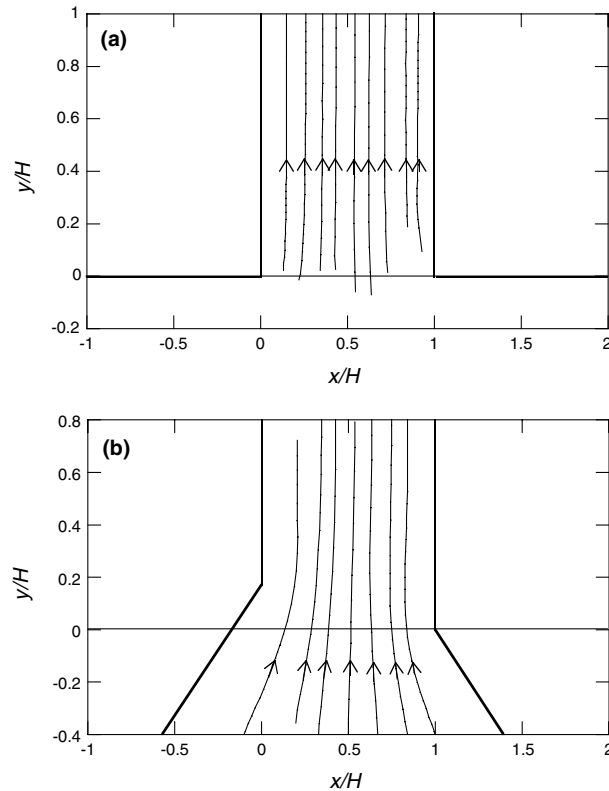
Fig. 4. (a) Entrance-region trajectories for sample small particles with $0.07 \leqslant d_{\mathrm{p}}/H \leqslant 0.10$ in the blunt-entrance channel, where x is the distance across the channel and y is the distance along the channel. Particles are focused away from the walls and towards the center of channel. (b) Entrance-region trajectories for sample small particles with $0.07 \leqslant d_{\mathrm{p}}/H \leqslant 0.10$ in the angled-entrance channel. A slight skew of the trajectories towards the wall that begins at $y = 0.00$ and away from the wall that begins at $y = 0.17$ is observed.

fidence level). It is possible that inertial lift caused the large particles to drift toward the wall during the periods of high flow rate, since their centers are further from the wall than the equilibrium distance of $0.6(H/2)$, though the analysis of Segre and Silberberg (1961, 1962) is not strictly applicable to large particles with diameters comparable to the narrow dimension of the channel.

When a particle is very close to a wall, electrostatic interactions arising from electrical charges on the surfaces of the particles and the walls, as well as van der Waals forces between the particles and walls, may affect particle motion by influencing particle location across the channel width and particle motion along the channel length. The Debye decay length (Russel et al., 1989) for our solutions at pH 5.6 is about 0.2 μm. This distance corresponds to 0.4%, 0.08% and 0.05% of the small, medium and large particle median diameters, respectively. The smallest particle-wall gap calculated from the measured particle locations and velocities (Fig. 2) is several times larger than this value, at least 5 μm for the smallest particles and 0.5 μm for the largest particles, indicating that the electrostatic repulsion between the particle and the wall would be shielded for virtually all of the experiments. Moreover, considering a van der Waals attractive force of
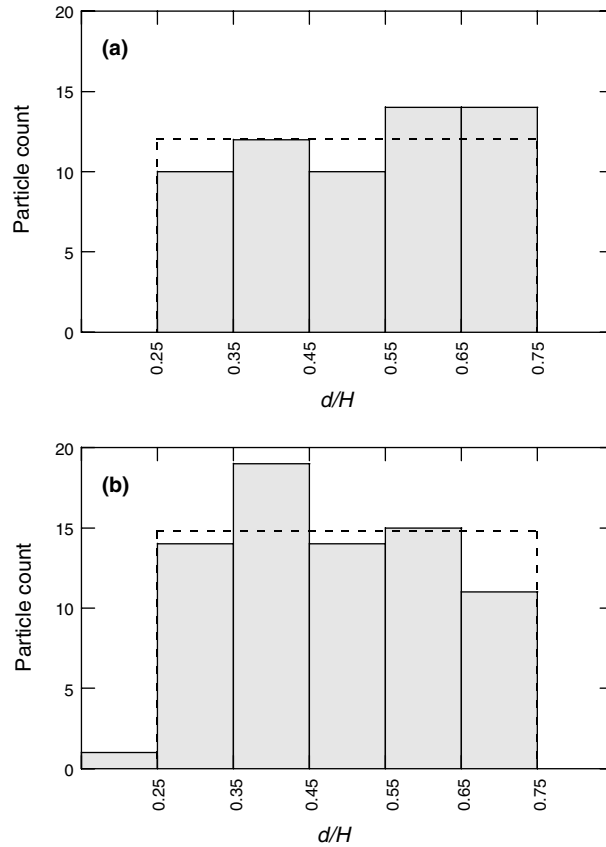
Fig. 5. (a) Frequency distribution of particles with $0.46 \leqslant d_p/H \leqslant 0.54$ in the blunt-entrance channel. (b) Frequency distribution of same size range of particles in the angled-entrance channel with right wall extending into entrance region. The dashed line in each plot is a uniform distribution of particles across the channel width for the number of particles in a given plot, except for the excluded region within one average particle radius of either wall. The one particle in the left-most bin of Fig. 5b is smaller than the average size.

$F_A = Aa/6h^2$ (Hiemenz, 1986) balanced by a viscous lubrication resistance force of $F_L = 6\pi\mu a^2 U_A/h$ (Russel et al., 1989), where h is the gap between the particle and the nearby wall, the normal velocity of the particle toward the wall due to van der Waals attraction is $U_A = A/(36\pi\mu ah)$, ignoring the effect of the second wall as a first approximation (the second wall would only act to slow the attractive motion of the particle toward the closer wall). Choosing a typical value of $A = 7 \times 10^{-21}$ J (Russel et al., 1989), $U_A = 3 \times 10^{-8}$ cm/s for either the smallest particles ($a = 23$ μm, $h = 5$ μm) or the largest particles ($a = 220$ μm, $h = 0.5$ μm) at closest approach, indicating that the lateral motion toward the wall is negligible during the observation period (typically 30–60 s). The surface charge of the wall would also yield a streaming potential, which is an electric field induced by fluid moving past a charged surface. A typical zeta potential for PMMA is 30 mV (Kirby and Hasselbrink, 2004), yielding an induced electric field (Russel et al., 1989) of 3×10^{-6} V/cm. Using this value in the expression for the electrophoretic velocity of a particle
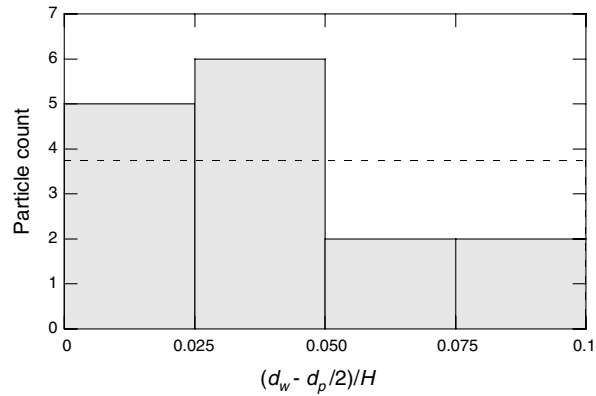
Fig. 6. Frequency distribution of particles with $0.79 \leqslant d_p/H \leqslant 0.83$ as a function of the gap from the nearest wall, $(d_w - d_p/2)/H$, where d_w is the distance to the nearest wall, d_p is the particle diameter, and H is the channel width.

(Russel et al., 1989) with the 40 mV potential of polystyrene (Vos et al., 2001) yields a negligibly small electrophoretic velocity of 5×10^{-12} cm/s.

3.4. Average particle velocities

The average velocity for a distribution of particles is of interest for applications that involve pulse inputs of particles and reagents, where the particles and reagents need to remain in close proximity for a defined time after input (e.g., an application in which cell lysis needs to occur). Fig. 7 shows the average particle velocity, $\langle U_p \rangle$, calculated using the measured velocities in Fig. 2, as compared to the predicted average particle velocity for a uniform distribution of particles across the channel (Staben et al., 2003). These values are scaled by the average fluid velocity, $\langle U_f \rangle = (2/3)U_c$. The horizontal error bars on Fig. 7 represent the range of particle sizes used to obtain the data point (e.g., the medium particle points include $0.46 \leqslant d_p/H \leqslant 0.54$). The vertical error bars represent the 90% confidence intervals on the mean.

The experimental data exceed the predicted value of the average particle velocity for the smallest particles, because the predicted value is based on a uniform distribution of particle centers across the channel (except within the excluded regions within one particle radius of either wall), while the experimental values are for distributions that have a deficit of particles on the slow-moving streamlines near the walls but outside the excluded region (see Fig. 3). As expected, the difference is larger for the blunt entrance than for the angled entrance, as the former yields a greater deficit of the small particles near the wall. The medium particles show excellent agreement between theory and experiment for the blunt entrance, as the measured distribution is nearly uniform in this case (Fig. 5a). The average velocity of the medium particles is again slightly lower for the angled entrance than for the blunt entrance, as there are more particles translating with slow velocities very close to the wall for the angled entrance (see Fig. 2).

While the average particle velocity exceeds the average fluid velocity for the small and medium particles, due to particle exclusion from the slow-moving, near-wall region, the average velocity of the large particles is lower than the average fluid velocity, due to the retarding effects of both
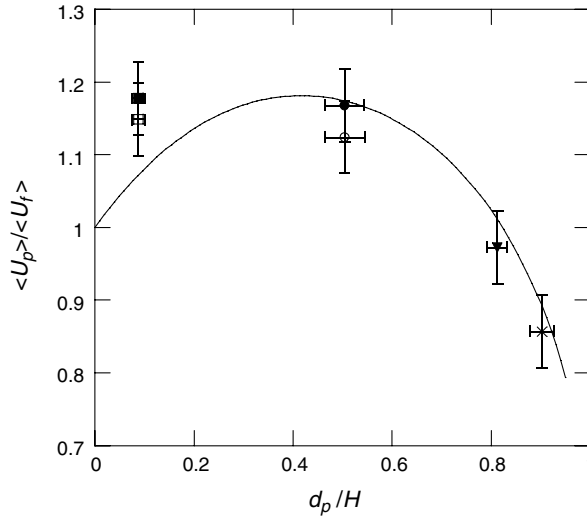
Fig. 7. Average particle velocity, $\langle U_{\mathrm{p}} \rangle$, relative to the average fluid velocity, $\langle U_{\mathrm{f}} \rangle$, versus dimensionless particle diameter, d_{p}/H, in a two-dimensional channel with Poiseuille flow. The solid curve is the simulation result (Staben et al., 2003) for a uniform distribution of particles across the channel; the symbols are for particles in the blunt-entrance channel with $0.07 \leqslant d_{\mathrm{p}}/H \leqslant 0.10$ (■) and $0.46 \leqslant d_{\mathrm{p}}/H \leqslant 0.54$ (●); in the angled-entrance channel with $0.07 \leqslant d_{\mathrm{p}}/H \leqslant 0.10$ (□) and $0.46 \leqslant d_{\mathrm{p}}/H \leqslant 0.54$ (○); and in both channels for $0.79 \leqslant d_{\mathrm{p}}/H \leqslant 0.83$ (▼) and $0.88 \leqslant d_{\mathrm{p}}/H \leqslant 0.93$ (×). The error bars along the *x*-axis represent the range of particle sizes used for the given data point, while the error bars along the *y*-axis represent the 90% confidence intervals about the mean.

walls. All velocity measurements for particles with $0.79 \leqslant d_{\mathrm{p}}/H \leqslant 0.83$ from both entrance geometries are combined in Fig. 7, since the number of measurements in each of the separate subgroups in this range in Fig. 2 is not large enough to yield an accurate result. A similar grouping is applied for data with $0.88 \leqslant d_{\mathrm{p}}/H \leqslant 0.93$. For these large particles, the experimental results are slightly below the predicted curve, due to the slight excess of particles very close to one of the walls (Fig. 6).

The maximum in the theory curve results from the competition between the wall effects and the exclusion of particles from the region within one particle radius of either wall. The smallest particles move with the fluid and, hence, have an average velocity that is similar to the average fluid velocity. Medium particles are excluded from the slow-moving fluid velocities near the walls and are only slightly retarded by the presence of the walls, which leads to the maximum average particle velocity in the predicted curve of $\langle U_{\mathrm{p}} \rangle / \langle U_{\mathrm{f}} \rangle = 1.18$ at $d_{\mathrm{p}}/H = 0.42$. Large particles are substantially slowed by the presence of the walls, which overwhelms any increase in the average velocity caused by the exclusion of the centers from the region within one radius of the walls, leading to a predicted average particle velocity that is less than the average fluid velocity for particles with $d_{\mathrm{p}}/H \geqslant 0.82$.

Small particles move with the fluid and have a wide range of possible particle velocities, as evidenced from Fig. 2. This wide range of velocities will lead to considerable convective spreading of the small particles. Large particles, on the other hand, have a narrow range of particle velocities. For particles with $d_{\mathrm{p}}/H \approx 0.8$, $\langle U_{\mathrm{p}} \rangle / \langle U_{\mathrm{f}} \rangle \approx 1$, which means that a pulse input of particles of this

size (e.g., cells) and reagent will experience minimal longitudinal spreading and would remain in close proximity while they travel along the channel length.

4. Conclusions

In this work, we have compared experimentally measured particle velocities for a range of spherical particle sizes to our previous boundary-integral simulations (Staben et al., 2003) for spheres translating in Poiseuille flow between two parallel walls. Good agreement between theory and experiment was obtained for small particles ($0.07 \leqslant d_\mathrm{p}/H \leqslant 0.10$), medium particles ($0.46 \leqslant d_\mathrm{p}/H \leqslant 0.54$) and large particles ($0.79 \leqslant d_\mathrm{p}/H \leqslant 0.95$). The larger particles are retarded more by the channel walls than are the smaller particles with the same center location across the channel. However, larger particles have a more narrow distribution of particle velocities, due to the exclusion of particles from the slow-moving streamlines within one particle radius of either wall.

In addition to validating our model, we examined the effects of entrance geometry upon the distribution of particles across the narrow dimension of a large-aspect-ratio microchannel. A blunt-entrance geometry, in which the parallel-wall section of the channel begins at the entrance of the channel, was seen to provide a significant amount of focusing of small particles away from the walls and towards the center of the channel, as evidenced in particle-distribution histograms. For channels with an angled-entrance region, the particle distribution is more uniform across the channel, but the particles are skewed slightly towards the side of the channel encountered first in the entrance region. The medium-size particles have nearly uniform distributions across the channel for both entrance geometries, whereas the limited number of large particles shows a slight bias toward being located close to a wall.

The individual particle velocities were used to obtain average particle velocities for the two entrance geometries, which were compared to the predicted average velocities for a uniform distribution of particles. For the small particles, the average particle velocity from the experimental data is greater than the predicted average particle velocity, due to the nonuniform distribution of particle locations in the experiments. Also, the blunt-entrance average velocity is higher than the angled-entrance average velocity, since the blunt entrance shifts particles towards the center of the channel, while the offset-angled entrance shifts particles away from one wall but does not significantly affect the overall uniformity of the distribution near the other wall.

A practical finding from this work is that $\langle U_\mathrm{p} \rangle / \langle U_\mathrm{f} \rangle \approx 1$ when $d_\mathrm{p}/H \approx 0.8$, indicating that particles and soluble reagent entering a microfluidic channel together will remain together as they travel down a channel designed such that $d_\mathrm{p}/H \approx 0.8$. Moreover, the range of particle velocities under these conditions is relatively small (see triangles in Fig. 2) and so not much particle spreading will occur (the reagent spreading will be governed by Taylor dispersion and may be controlled to be of similar magnitude to the particle spreading).

Acknowledgements

References

Andersson, H., van der Wijngaart, W., Nilsson, P., Enoksson, P., Stemme, G., 2001. A valve-less diffuser micropump for microfluidic analytical systems. Sensors and Actuators B—Chemical 72, 259–265.

Beebe, D.J., Mensing, G.A., Walker, G.M., 2002. Physics and applications of microfluidics in biology. Annu. Rev. Biomed. Eng. 4, 261–286.

Beebe, D.J., Moore, J.S., Bauer, J.M., Yu, Q., Liu, R.H., Devadoss, C., Jo, B.H., 2000. Functional hydrogel structures for autonomous flow control inside microfluidic channels. Nature 404, 588–590.

Brody, J.P., Yager, P., Goldstein, R.E., Austin, R.H., 1996. Biotechnology at low Reynolds numbers. Biophys. J. 71, 3430–3441.

Cox, R.G., Mason, S.G., 1971. Suspended particles in fluid flow through tubes. Annu. Rev. Fluid Mech. 3, 291–316.

Davis, R.H., 1992. Modeling of fouling of cross-flow microfiltration membranes. Sep. Purif. Methods 21, 75–126.

Devasenathipathy, S., Santiago, J.G., Takehara, K., 2002. Particle tracking techniques for electrokinetic microchannel flows. Anal. Chem. 74, 3704–3713.

Ehrlich, D.J., Matsudaira, P., 1999. Microfluidic devices for DNA analysis. Trends Biotechnol. 17, 315–319.

Eteshola, E., Leckband, D., 2001. Development and characterization of an ELISA assay in PDMS microfluidic channels. Sensors and Actuators B—Chemical 72, 129–133.

Eyal, S., Quake, S.R., 2002. Velocity-independent microfluidic flow cytometry. Electrophoresis 23, 2653–2657.

Good, B.T., Bowman, C.N., Davis, R.H., 2004. Modeling and verification of fluid-responsive polymer pumps for microfluidic systems. Chem. Eng. Sci. 59, 5967–5974.

Happel, J., Brenner, H., 1986. Low Reynolds Number Hydrodynamics. Martinus Nijhoff, Dordrecht.

Hiemenz, P.C., 1986. Principles of Colloid and Surface Chemistry. Marcel Dekker, Inc., New York.

Ho, B.P., Leal, L.G., 1974. Inertial migration of rigid spheres in 2-dimensional unidirectional flows. J. Fluid Mech. 65, 365–400.

Jackson, W.C., Kuckuck, F., Edwards, B.S., Mammoli, A., Gallegos, C.M., Lopez, G.P., Buranda, T., Sklar, L.A., 2002. Mixing small volumes for continuous high-throughput flow cytometry: Performance of a mixing Y and peristaltic sample delivery. Cytometry 47, 183–191.

Kirby, B.J., Hasselbrink, E.F., 2004. Zeta potential of microfluidic substrates: 2. Data for polymers. Electrophoresis 25, 203–213.

Koch, M., Evans, A.G.R., Brunnschweiler, A., 1999. Design and fabrication of a micromachined Coulter counter. J. Micromech. Microeng. 9, 159–161.

Liu, R.H., Stremler, M.A., Sharp, K.V., Olsen, M.G., Santiago, J.G., Adrian, R.J., Aref, H., Beebe, D.J., 2000. Passive mixing in a three-dimensional serpentine microchannel. J. Microelectromech. Systems 9, 190–197.

Russel, W.B., Saville, D.A., Schowalter, W.R., 1989. Colloidal Dispersions. Cambridge University Press, Cambridge.

Segre, G., Silberberg, A., 1961. Radial particle displacements in Poiseuille flow of suspensions. Nature 189, 209–210.

Segre, G., Silberberg, A., 1962. Behaviour of rigid macroscopic spheres in Poiseuille flow. Part 2. Experimental results and interpretation. J. Fluid Mech. 14, 136–157.

Staben, M.E., Zinchenko, A.Z., Davis, R.H., 2003. Motion of a particle between two parallel plane walls in low-Reynolds-number Poiseuille flow. Phys. Fluids 15, 1711–1733.

Stroock, A.D., Dertinger, S.K.W., Ajdari, A., Mezic, I., Stone, H.A., Whitesides, G.M., 2002. Chaotic mixer for microchannels. Science 295, 647–651.

Terray, A., Oakey, J., Marr, D.W.M., 2002. Microfluidic control using colloidal devices. Science 296, 1841–1844.

Ukita, H., Kanehira, M., 2002. A shuttlecock optical rotator—its design, fabrication and evaluation for a microfluidic mixer. IEEE J. Sel. Top. Quantum Electronics 8, 111–117.

Unger, M.A., Chou, H.P., Thorsen, T., Scherer, A., Quake, S.R., 2000. Monolithic microfabricated valves and pumps by multilayer soft lithography. Science 288, 113–116.

Vasseur, P., Cox, R.G., 1976. The lateral migration of a spherical-particle in two-dimensional shear flows. J. Fluid Mech. 78, 385–413.

Vos, R., Lux, M., Xu, K., Fyen, W., Kenens, C., Conard, T., Mertens, P., Heyns, M., Hatcher, Z., Hoffman, M., 2001. Removal of submicrometer particles from silicon wafer surfaces using HF-based cleaning mixtures. J. Electrochem. Soc. 148, G683–G691.

White, F., 1991. Viscous Fluid Flow. McGraw-Hill, New York.

Whitesides, G.M., Stroock, A.D., 2001. Flexible methods for microfluidics. Phys. Today 54, 42–48.

Zabow, G., Assi, F., Jenks, R., Prentiss, M., 2002. Guided microfluidics by electromagnetic capillary focusing. Appl. Phys. Lett. 80, 1483–1485.